Title
Biogenic gas nanostructures as ultrasonic molecular reporters.

Journal
Nature nanotechnology, 9(4)

ISSN
1748-3387

Authors
Shapiro, Mikhail G
Goodwill, Patrick W
Neogy, Arkosnato
et al.

Publication Date
2014-04-01

DOI
10.1038/nnano.2014.32

Peer reviewed

Published in final edited form as:

Nat Nanotechnol. 2014 April ; 9(4): 311–316. doi:10.1038/nnano.2014.32.

Biogenic Gas Nanostructures as Ultrasonic Molecular Reporters

Mikhail G. Shapiro[1,2,3,#,*], **Patrick W. Goodwill**[2,4], **Arkosnato Neogy**[4], **Melissa Yin**[6], **F. Stuart Foster**[6,7], **David V. Schaffer**[2,5], and **Steven M. Conolly**[2,4]

[1]Miller Research Institute, University of California at Berkeley, Berkeley, CA, USA 94720

[2]Department of Bioengineering, University of California at Berkeley, Berkeley, CA, USA 94720

[3]Department of Molecular and Cell Biology, University of California at Berkeley, Berkeley, CA, USA 94720

[4]Department of Electrical Engineering and Computer Science, University of California at Berkeley, Berkeley, CA, USA 94720

[5]Department of Chemical and Biomolecular Engineering, University of California at Berkeley, Berkeley, CA, USA 94720

[6]Sunnybrook Research Institute, University of Toronto, Toronto, ON, Canada, M4N 3M5

[7]Department of Medical Biophysics, University of Toronto, Toronto, ON, Canada, M4N 3M5

Abstract

Ultrasound is among the most widely used non-invasive imaging modalities in biomedicine[1], but plays a surprisingly small role in molecular imaging due to a lack of suitable molecular reporters on the nanoscale. Here we introduce a new class of reporters for ultrasound based on genetically encoded gas nanostructures from microorganisms, including bacteria and archaea. Gas vesicles are gas-filled protein-shelled compartments with typical widths of 45–250 nm and lengths of 100–600 nm that exclude water and are permeable to gas[2, 3]. We show that gas vesicles produce stable ultrasound contrast that is readily detected *in vitro* and *in vivo*, that their genetically encoded physical properties enable multiple modes of imaging, and that contrast enhancement through aggregation permits their use as molecular biosensors.

[*]Correspondence to: M.G.S.: mikhail@caltech.edu.
[#]Current address: Division of Chemistry and Chemical Engineering, California Institute of Technology, Pasadena, CA 91125

Author Contributions MGS conceived and directed the study; planned the experiments; prepared the specimens; collected, analyzed and interpreted the data; and wrote the manuscript with input from all other authors. PWG designed and constructed the imaging instrument and accompanying signal processing software, and assisted with initial experiments. AN designed, constructed and optimized the imaging instrument and accompanying signal processing software. FSF and MY designed, performed and analyzed the data from intravenous injection experiments. All the authors provided input on study and experimental design, data analysis, data interpretation and the manuscript.

Additional Information Supplementary information accompanies this paper at www.nature.com/naturenanotechnology.

Competing Financial Interests F. Stuart Foster is a consultant to VisualSonics. The authors declare no other competing financial interests.

Contrast-enhanced ultrasound has been an active area of research and development for over 40 years[4], with conventional ultrasound contrast agents formulated as lipid- or protein-stabilized gas microbubbles. The partial pressure gradient between a microbubble's gas interior and surrounding media, which is inversely proportional to its radius, limits most microbubbles to sizes larger than one micron and leads to gas escape, bubble fragmentation and collapse after *in vivo* administration[5, 6]. Although microbubbles have been very successful in clinical imaging of the blood pool and related physiology[7], and have recently been proposed as potential cell-internalized labels[8], several factors limit their range of applications in molecular imaging. For example, microbubbles of micron size are typically limited to imaging targets within the vasculature. In addition, microbubbles typically have a short half-life compared to the *in vivo* dynamics of immune, stem and other cells[5, 7, 9]. Furthermore, none of the solid[10], liquid[11], hollow[12] or phase-change[13] contrast agents proposed as microbubble alternatives have so far become widely adopted due to limitations in echogenicity, stability or ease of synthesis. As a result, important studies in oncology, immunology, regenerative medicine and other biomedical areas remain dominated by nanoparticle reporters designed for optical, magnetic resonance and nuclear imaging[14].

We hypothesized that nanoscale reporters with novel properties for molecular ultrasonography could be derived from natural biological structures. In particular, we considered gas vesicles (GVs), genetically encoded gas nanostructures formed by certain bacteria and archaea as a means to control buoyancy for optimal access to light and nutrients[2, 3]. GVs have cylindrical or biconical shapes, with maximal diameters of 45–250 nm and typical lengths of 100–600 nm varying between genetic hosts [2, 3]. These nanostructures interact with gases through a fundamentally different mechanism than microbubbles. Whereas microbubbles trap pre-loaded gas, GVs exclude water but permit gas from the surrounding media to freely diffuse in and out of their 1–10 attoliter interior through a 2 nm protein shell[2] (Fig. 1a). As a result, no pressure gradient exists between the inside and outside of GVs, permitting them to be inherently stable despite their nanometer size. Although they were discovered over 100 years ago[15] and have been well-characterized biophysically[2], GVs have yet to be substantially exploited as a nanotechnology[3]. We hypothesized that GVs could serve as nanoscale molecular reporters for ultrasound imaging, and furthermore that their genetically encoded structural properties, such as collapse at specific hydrostatic pressures, could enable new imaging modes beyond those available with microbubbles.

To test this hypothesis, GVs from *Anabaena flos-aquae* (*Ana*) and *Halobacterium NRC-1* (*Halo*) (Fig. 1, b–c), representing two genetically distant sources[3], were purified through tonic cell lysis and centrifugally assisted floatation and imaged in gel phantoms using a scanning single-element ultrasound imaging system operating at 4.8 MHz, 8.6 MHz and 17 MHz (for sample preparation and imaging details, see Methods). GVs from both species produced robust contrast relative to buffer controls at optical densities (OD) ranging from 0.25 to 2.0 (Fig. 1d–g), corresponding to nanostructure concentrations of 150 pM to 1.2 nM (*Ana*) or 5 pM to 40 pM (*Halo*), and gas volume fractions of approximately 0.01% to 0.1%. GV echogenicity in this configuration was detectable for over one week (Supplementary Fig. 1). Contrast was strongest at the highest frequency, with OD 2.0 *Ana* GVs producing

27.0 ± 4.1 greater scattering than buffer controls (Fig. 1f). The balance of scattering and attenuation differed between *Ana* and *Halo* GVs. Whereas *Ana* GVs produced backscatter fairly uniformly along the axial dimension (from top to bottom in Fig. 1d), *Halo* GVs at higher concentrations produced acoustic attenuation, manifesting as reduced signal beneath the gas vesicles in the gel phantom (Fig. 1e, Supplementary Fig. 2).

GVs can be collapsed by rapidly increasing the hydrostatic pressure past a species-specific critical point ranging from 40 kPa to over 700 kPa [2, 16] (Fig. 1b–c). GVs that were hydrostatically collapsed prior to loading into the phantom failed to show ultrasound contrast, confirming the echogenic role of their gas compartments (Fig. 1, d–e).

Non-linear imaging modes relying on harmonic signals have been used to improve the contrast specificity of microbubble-enhanced ultrasound[17]. In particular, harmonic backscatter is thought to arise from oscillations in microbubble radius[18] in response to incident pressure waves. We tested whether harmonics could also be detected from GVs. Transmitting at 6 MHz, we observed substantial second and third harmonic signals in *Halo* GVs at 12 MHz and 18 MHz compared to polystyrene microspheres, a linear scattering reference material (Fig. 2a). *Ana* GVs did not produce harmonic signals at 6 MHz (Supplementary Fig. 3). Images formed by processing *Halo* GV signals through band-pass filters centered at the second and third harmonics showed 3.7-fold and 4.6-fold greater contrast enhancement in GV-containing wells relative to the linear scatterer than did images processed at the transmit frequency (Fig. 2b, c). To further explore GV-specific contrast enhancement, we took advantage of pressure-induced GV collapse by testing its application *in situ* at ultrasound frequencies. *Halo* and *Ana* GVs were imaged before and after a disruptive scan at 8.6 MHz in which the transducer output was set to produce a peak pressure of 650 kPa – above the critical collapse level of both species of GVs (70–150 kPa for *Halo* and 440–605 kPa for *Ana*)[16] (Fig. 2d). The GV signal was thereby mostly eliminated, enabling the generation of subtraction images in which the signal from *Halo* and *Ana* GV wells relative to polystyrene was boosted by factors of 10 and 22, respectively. (Fig. 2d, e). Such subtraction images can be used to increase the specificity of contrast information relative to background scattering[19].

The fact that GVs from different species have distinct critical collapse pressures[16] raised the further prospect of distinguishing multiple populations of GVs in the same sample through “serial collapse” imaging. In this paradigm, contrast originating from GVs with a low collapse pressure is identified by its disappearance upon the application of pressure pulses with amplitudes above their critical point but below that of other GVs. The remaining contrast is attributable to GV species with higher collapse pressures. To test this paradigm with our two species of GVs, we prepared imaging phantoms with wells containing *Halo* GVs, *Ana* GVs or a combination of both (Fig. 2f). In an initial image, both populations of GVs produce contrast (Fig 2f, top), but after low-pressure collapse at 300 kPa, contrast in the *Halo* GV well is eliminated and contrast in the mixed well is reduced (Fig 2f, middle). After high-pressure collapse at 650 kPa, contrast in the *Ana* GV well and the mixed well is also eliminated, leaving only background (Fig 2f, bottom). *Halo* GV contrast can now be inferred by subtracting the second image from the first image (Fig 2g, top) and *Ana* GV contrast can be calculated by subtracting the third image from the second image (Fig 2g,

bottom). An overlay correctly shows the mixed well as containing both types of GVs (Fig. 2h).

Because GVs are smaller than the wavelengths typically used in ultrasound, we further hypothesized that assemblies of GV nanoparticles would produce enhanced scattering compared to un-aggregated solutions, as previously shown with perfluorocarbon droplets[11], potentially enabling GVs to serve as biomolecular sensors analogous to aggregation-dependent nanoparticle reporters for magnetic resonance imaging (MRI)[20]. To test this possibility, we functionalized the surface of *Ana* GVs with biotin and exposed them to various quantities of free streptavidin. In the absence of streptavidin, or at streptavidin concentrations sufficient to saturate surface biotins, GVs are expected to remain unaggregated; however, at intermediate concentrations, streptavidin is expected to mediate GV clustering (Fig. 3a). The formation of aggregates (~1 μm) in response to streptavidin was confirmed by TEM (Fig. 3d), and at higher magnification it was also possible to discern individual streptavidin molecules on the surface of GVs at the expected relative densities (arrows in Fig. 3d). When nanoparticle assemblies were imaged in ultrasound, the intermediate streptavidin concentration was detected by a two-fold increase in contrast (Fig. 3b, c). *Ana* GVs were chosen for functionalization because their greater resistance to collapse (compared to *Halo* GVs) allows easier handling during repeated purifications.

Next, to test the feasibility of using GVs expressed inside cells as intracellular reporters or genetic labels, we imaged intact *Ana* cells and compared the resulting contrast to GVs that were released from the same quantity of cells through hypertonic lysis (Fig. 3e–g). The intact cells exhibited a 12-fold stronger signal, indicating that intracellular GVs have the potential to serve as genetically encoded reporters or dynamic indicators of cellular integrity. The quantity of GVs recovered after lysis (815 ± 124 μL gas volume per g of dry cell pellet, N=4) was greater than previously measured intracellular GV contents (~350–500 μL/g)[21, 22], suggesting that the observed difference in contrast between intact and lysed cells is unlikely to arise from GV destruction during lysis.

Finally, to demonstrate that GVs are capable of producing ultrasound contrast *in vivo*, we performed subcutaneous and intravenous injections of *Halo* GVs into live anaesthetized mice, choosing *Halo* GVs for their robust non-linear signals (Fig. 2a). We first injected the GVs or a buffer control subcutaneously in the lower abdomen of anesthetized CD-1 mice, and acquired second-harmonic images (transmitting at 6 MHz) using our single-element apparatus. We observed robust enhancement on the GV side (Fig. 4a, b, d), but not on the control side. To confirm that GVs were the source of the observed contrast, we applied ultrasonic pulses at a supra-collapse pressure (650 kPa), resulting in contrast disappearance (Fig. 4c, d). Regions of interest containing GVs exhibited 60 ± 14% stronger backscattered signals than buffer-injected controls ($p = 0.008$); this difference disappeared after collapse ($p = 0.23$). Images from five animals are shown in Supplementary Fig. S4. In addition, we used a commercial high frequency small animal ultrasound scanner operating at 18 MHz to image the dynamics of *Halo* GVs (50 μL, OD 6.0) injected into the tail vein of severe-combined immunodeficient (SCID) nude mice. Five seconds after the start of the injection (at a rate of 0.6 mL/min), robust scattering was observed from the inferior vena cava in non-linear contrast images (Fig. 4 e, h, i and Supplementary Movie S1). Then, as expected for

unfunctionalized nanostructures, GV contrast accumulated in the liver, reaching a steady state after approximately 50 seconds (Fig. 4 f, h, j and Supplementary Movie S1). Application of a high-power burst from the transducer completely eliminated the accumulated contrast (Fig. 4 g, h, i, j and Supplementary Movie S1). Under these conditions, GVs were detectable *in vivo* when injected at concentrations as low as OD 1.5 in the inferior vena cava (Fig. 4k), and OD 3.0 in the liver (Fig. 4l); contrast increased with dosing above these levels.

No acute toxicity was observed in the intravenously injected mice. The animals' heart rate and breathing remained normal during and after imaging (Supplementary Fig. S5), and no significant decrease in five veterinary health measures (activity, weight, food intake, posture and hydration) was observed immediately or 24 and 48 hours after GV administration (Supplementary Table S2). GVs taken up by the liver appeared to be degraded within 60 minutes of uptake (Supplementary Fig. S6) consistent with other protein nanostructures cleared by this organ, e.g. bacteriophage[23]. However, when GVs were injected subcutaneously, occupying a tissue that lacks rapid nanoparticle clearance and protein degradation, they produced stable contrast for at least two hours (Supplementary Fig. S7).

Our findings establish GVs as a promising new class of molecular reporters for ultrasonography. Their ability to produce stable contrast at sub-nanomolar reporter concentrations may enable future applications of ultrasound in imaging studies that, to date, have been dominated by nanoparticle reporters for other modalities such as MRI and fluorescence[14]. These concentrations represent gas contents (< 1 μL gas / mL solution) similar to or smaller than those of typical formulations of microbubbles, which contain approximately 10^3 times more gas per particle[19]. Furthermore, several of the demonstrated acoustic properties, including response at high frequencies (up to the measured 18 MHz), ability to produce harmonic signals (in *Halo* GVs) and controlled acoustic collapsibility *in situ*, are especially advantageous for high-resolution contrast-enhanced imaging[24]. Future work is needed to determine how these properties are influenced by the specific size, shape, elasticity, gas diffusivity and collapse-resistance of these nanostructures. Some insights may be gained by refining existing microbubble theories, which predict peak responses at frequencies > 18 MHz for contrast agents with submicron size and relatively high stiffness[18, 25–27]. In addition, differences in the physical properties of GVs obtained from distinct species, such as sharply tuned collapse pressures and harmonic scattering, may enable new detection schemes, as shown here with serial collapse imaging of GVs from *Ana* and *Halo*.

Application-specific reporters can be generated by functionalizing the surface of GVs through bioconjugation, as shown here with clustering-based analyte (streptavidin) detection by biotinylated *Ana* GVs. The nanometer dimensions of these structures may enable the labeling of targets outside the bloodstream, for example tumours with increased vascular permeability[28], to be explored in future studies. As with other nanoscale imaging agents, PEGylation or other surface treatments may be necessary to increase circulation time, reduce clearance by organs such as the liver and decrease immunogenicity[29]. Future work is also needed to demonstrate the safety of GVs for potential clinical and pre-clinical applications, including ones that may require repeated administration.

Intriguingly, the intracellular detectability of GVs suggests that they could in the future be developed as reporter genes for bacterial or mammalian cell tracking, potentially enabling longer-term monitoring than recently demonstrated with microbubbles[8]. Indeed, gene clusters encoding GVs have already been heterologously expressed in *Escherichia coli* [30]. Furthermore, genetic sequence control over the size, shape and collapse pressures of GVs in their native hosts[3] could assist with the optimization of GV properties for future use as either injectable or encoded reporters.

Finally, we note that GVs' well-defined molecular structures, anisotropic shapes, hollow interiors, gas permeability, optical scattering, buoyancy, chemical reactivity, controlled collapse and genetic encoding could conceivably make them useful in various other nanotechnology applications.

Methods

Additional details are provided in the Supplementary Information.

Gas vesicle preparation

Anabaena flos-aquae (*Ana*) was cultured in Gorham's media at room temperature under office fluorescent lighting. *Halobacteria NRC-1* (*Halo*) was cultured with shaking at 37°C in ATCC medium 2185, under ambient light. GVs were isolated from *Ana* and *Halo* using hypertonic and hypotonic lysis, respectively, and purified by repeated centrifugally-assisted flotation (Supplementary Fig. S8). Pre-collapsed GVs were prepared through the application of hydrostatic pressure in a capped syringe.

The concentration of GVs was estimated based on pressure-sensitive optical density at 500 nm ($OD_{500,PS}$)[2]. The relationship between $OD_{500,PS}$ and protein concentration was determined empirically using a total protein assay. Literature-based estimates of molecular weight[31–33] were used to calculate molar concentrations. Gas volume fractions were estimated using gas volumes of 8.4 μL/mg and 12.3 μL/mg for *Ana* and *Halo* GVs, respectively[32, 33].

For experiments comparing intact and lysed cells, *Ana* cultures (cell OD_{600nm} ~ 2) were mixed 50:50 with either water or 50% sucrose for 60 minutes before imaging. GVs release was measured using $OD_{500,PS}$ and compared to dry cell pellet weight.

Bio-functionalization and aggregation

Ana GVs were biotinylated using Sulfo-NHS-LC-Biotin and purified by 3X repeated floatation. For aggregation experiments, biotinylated GVs were mixed with streptavidin at indicated molar ratios for approximately 30 minutes before imaging.

In vitro ultrasound imaging

Imaging phantoms were prepared from 1% agarose in water. 2X concentrated GV samples were mixed 1:1 with melted 1% agarose, and 100uL of the mixture was quickly loaded into phantom wells. The same procedure was used to load polystyrene microspheres (0.83% final w/v, 4.78 μm). Imaging was performed using a home-built imaging setup. A 5 MHz, 10

MHz or 20 MHz single element transducer (6.3, 6.3 and 3.2 mm active areas, respectively; 25.4 mm focal distance) was mounted on a computer-controlled 2D translating stage, immersed in water approximately 20 mm above the sample. A programmable pulse generator and radio frequency amplifier drove transducers at specified frequencies with sinusoidal pulse trains of approximately 1 μs. The pre-amplifier function of a pulse-receiver with high-pass and low-pass filtering at 5 MHz and 75 MHz, connected to an oscilloscope, was used to collect ultrasound signals and record them using MATLAB (Mathworks, Natick, MA). *In situ* GV collapse was obtained by repeated pulsing at indicated pressures at 8 or 8.6MHz.

Image analysis

MATLAB was used to process raw time-domain data into two-dimensional (B-mode) images. If multiple neighboring lines perpendicular to the B-mode image were acquired, they were averaged. Regions of interest were defined manually in the axial dimension and automatically in the lateral dimension. Processing and scaling parameters are listed in Supplementary Table 1. Colour maps used in the images are shown in Supplementary Figure S9. Power spectra represent squared absolute values of fast Fourier transforms of raw time-domain signals.

In vivo imaging

For imaging of subcutaneously injected GVs (Fig. 4a–d) female CD-1 mice under isoflurane anesthesia were depilated above the lower abdomen and injected subcutaneously with 150uL *Halo* GVs (OD 6) on one side and 150uL PBS on the other side of the abdomen. An ultrasonic transducer was coupled through a column of ultrasound gel above the injected region and scanned or used to apply destructive pulses as described above.

Intravenously injected GVs were imaged in SCID nude mice using the VisualSonics Vevo 2100 high frequency ultrasound scanner operating in non-linear contrast mode, with the MS250 transducer set to 18 MHz and 2% power. The mice were maintained under isoflurane anesthesia on a heated imaging platform. Breathing and heart rate were monitored by built-in sensors. During infusion experiments, images were acquired continuously at a frame rate of 15frames/sec for approximately 100 seconds. 50 μL of *Halo* GVs in PBS were infused approximately 10 seconds after the start of the experiment at a flow rate of 0.6 mL/min. After 65 seconds, a burst pulse was applied to collapse the GVs. ROIs were analyzed using Vevo Lab software. Smoothed infusion time course curves were generated using locally weighed scatterplot smoothing. AUC values were obtained from raw data normalized to the pre-infusion baseline. *Halo* GVs remaining in the liver following intravenous injection were imaged as described above, with the additional collection of images during 30-second windows at 15, 30, 45, 60 and/or 75 minutes after injection. In subcutaneous injection experiments, 100 μL OD 6.0 *Halo* GVs were injected subcutaneously on the right side of the abdomen and 100 μL PBS was injected contralaterally.

Veterinary evaluation

Animals were evaluated by a veterinarian on a 15-point scale comprising three points each for activity, weight, food intake, posture and hydration. The veterinarian was blinded to the injection group.

TEM

TEM images were obtained on a Philips/FEI (Hillsboro, OR) Tecnai 12 microscope operating at 120kV. GV samples (OD 0.1) were deposited on a carbon-coated formvar grid and stained with 2% uranyl acetate.

Supplementary Material

Refer to Web version on PubMed Central for supplementary material.

Acknowledgements

The authors thank P. Lum for ultrasound equipment and advice, R. Zalpuri and K. McDonald for assistance with electron microscopy, K-K. Park and P. Khuri-Yakub for assistance with hydrophone measurements, E. Chérin for input on *in vivo* experiments and the manuscript, and A. Bar-Zion for assistance with data analysis. M.G.S. acknowledges funding from the Miller Research Institute and the Burroughs Wellcome Career Award at the Scientific Interface. Other funding was provided by California Institute for Regenerative Medicine grant RT2-02022 (D.V.S.), National Institutes of Health grant R01EB013689 (S.M.C), the Canadian Institutes of Health Research (F.S.F.) and the Terry Fox Foundation (F.S.F.).

References

1. Smith-Bindman R, et al. Use of diagnostic imaging studies and associated radiation exposure for patients enrolled in large integrated health care systems, 1996–2010. JAMA. 2012; 307:2400–2409. [PubMed: 22692172]
2. Walsby AE. Gas vesicles. Microbiol. Rev. 1994; 58:94–144. [PubMed: 8177173]
3. Pfeifer F. Distribution, formation and regulation of gas vesicles. Nat. Rev. Microbiol. 2012; 10:705–715. [PubMed: 22941504]
4. Gramiak R, Shah PM, Kramer DH. Ultrasound cardiography - contrast studies in anatomy and function. Radiology. 1969; 92:939–948. [PubMed: 5771834]
5. Ferrara K, Pollard R, Borden M. Ultrasound microbubble contrast agents: fundamentals and application to gene and drug delivery. Annu. Rev. Biomed. Eng. 2007; 9:415–447. [PubMed: 17651012]
6. Kaufmann BA, Lindner JR. Molecular imaging with targeted contrast ultrasound. Curr. Opin. Biotechnol. 2007; 18:11–16. [PubMed: 17241779]
7. Cosgrove D, Harvey C. Clinical uses of microbubbles in diagnosis and treatment. Med. Biol. Eng. Comput. 2009; 47:813–826. [PubMed: 19205774]
8. Cui W, et al. Neural progenitor cells labeling with microbubble contrast agent for ultrasound imaging in vivo. Biomaterials. 2013; 34:4926–4935. [PubMed: 23578557]
9. Kircher MF, Gambhir SS, Grimm J. Noninvasive cell-tracking methods. Nat. Rev. Clin. Oncol. 2011; 8:677–688. [PubMed: 21946842]
10. Liu J, et al. Nanoparticles as image enhancing agents for ultrasonography. Phys. Med. Biol. 2006; 51:2179–2189. [PubMed: 16625034]
11. Lanza GM, et al. A novel site-targeted ultrasonic contrast agent with broad biomedical application. Circulation. 1996; 94:3334–3340. [PubMed: 8989148]
12. Martinez HP, et al. Hard shell gas-filled contrast enhancement particles for colour Doppler ultrasound imaging of tumors. Medchemcomm. 2010; 1:266–270. [PubMed: 21841967]

13. Kripfgans OD, Fowlkes JB, Miller DL, Eldevik OP, Carson PL. Acoustic droplet vaporization for therapeutic and diagnostic applications. Ultrasound Med. Biol. 2000; 26:1177–1189. [PubMed: 11053753]
14. James ML, Gambhir SS. A molecular imaging primer: modalities, imaging agents, and applications. Physiol. Rev. 2012; 92:897–965. [PubMed: 22535898]
15. Klebahn H. Gasvakuolen, ein Bestandteil der Zellen der wasserblutenbildenden Phycochromaceen. Flora (Jena). 1895; 80:241–282.
16. Walsby AE. Pressure relationships of gas vacuoles. Proc. R. Soc. B-Biol. Sci. 1971; 178:301–326.
17. Burns PN. Harmonic imaging with ultrasound contrast agents. Clin. Radiol. 1996; 51:50–55. [PubMed: 8605774]
18. de Jong N, Bouakaz A, Frinking P. Basic acoustic properties of microbubbles. Echocardiography. 2002; 19:229–240. [PubMed: 12022933]
19. Hauff, P.; Reinhardt, M.; Foster, S. Molecular Imaging I. Springer; 2008. p. 223-245.
20. Perez JM, Josephson L, O'Loughlin T, Hogemann D, Weissleder R. Magnetic relaxation switches capable of sensing molecular interactions. Nat. Biotechnol. 2002; 20:816–820. [PubMed: 12134166]
21. Oliver RL, Walsby AE. Direct evidence for the role of light-mediated gas vesicle collapse in the buoyancy regulation of anabaena flos-aquae (cyanobacteria). Limnol. Oceanogr. 1984; 29:879–886.
22. Kashyap S, Sundararajan A, Ju LK. Flotation characteristics of cyanobacterium Anabaena flos-aquae for gas vesicle production. Biotechnol. Bioeng. 1998; 60:636–641. [PubMed: 10099472]
23. Geier MR, Trigg ME, Merril CR. Fate of Bacteriophage Lambda in Non-immune Germ-free Mice. Nature. 1973; 246:221–222. [PubMed: 4586796]
24. Foster FS, Pavlin CJ, Harasiewicz KA, Christopher DA, Turnbull DH. Advances in ultrasound biomicroscopy. Ultrasound Med. Biol. 2000; 26:1–27. [PubMed: 10687788]
25. Frinking PJ, de Jong N. Acoustic modeling of shell-encapsulated gas bubbles. Ultrasound Med. Biol. 1998; 24:523–533. [PubMed: 9651962]
26. Hoff L, Sontum PC, Hovem JM. Oscillations of polymeric microbubbles: effect of the encapsulating shell. J. Acoust. Soc. Am. 2000; 107:2272–2280. [PubMed: 10790053]
27. Medwin H. Counting bubbles acoustically: a review. Ultrasonics. 1977; 15:7–13.
28. Yuan F, et al. Vascular permeability in a human tumor xenograft: molecular size dependence and cutoff size. Cancer Res. 1995; 55:3752–3756. [PubMed: 7641188]
29. Jokerst JV, Lobovkina T, Zare RN, Gambhir SS. Nanoparticle PEGylation for imaging and therapy. Nanomedicine. 2011; 6:715–728. [PubMed: 21718180]
30. Li N, Cannon MC. Gas vesicle genes identified in Bacillus megaterium and functional expression in Escherichia coli. J. Bacteriol. 1998; 180:2450–2458. [PubMed: 9573198]
31. Jost M, Jones DD, Weathers PJ. Counting of gas vacuoles by electron microscopy in lysates and purified fractions of microcystis aeruginosa. Protoplasma. 1971:329–335. [PubMed: 4331163]
32. Walsby AE, Armstrong RE. Average thickness of the gas vesicle wall in Anabaena flos-aquae. J. Mol. Biol. 1979; 129:279–285. [PubMed: 113551]
33. Yao AI, Facciotti MT. Regulatory multidimensionality of gas vesicle biogenesis in Halobacterium salinarum NRC-1. Archaea. 2011; 2011:716456. [PubMed: 22110395]

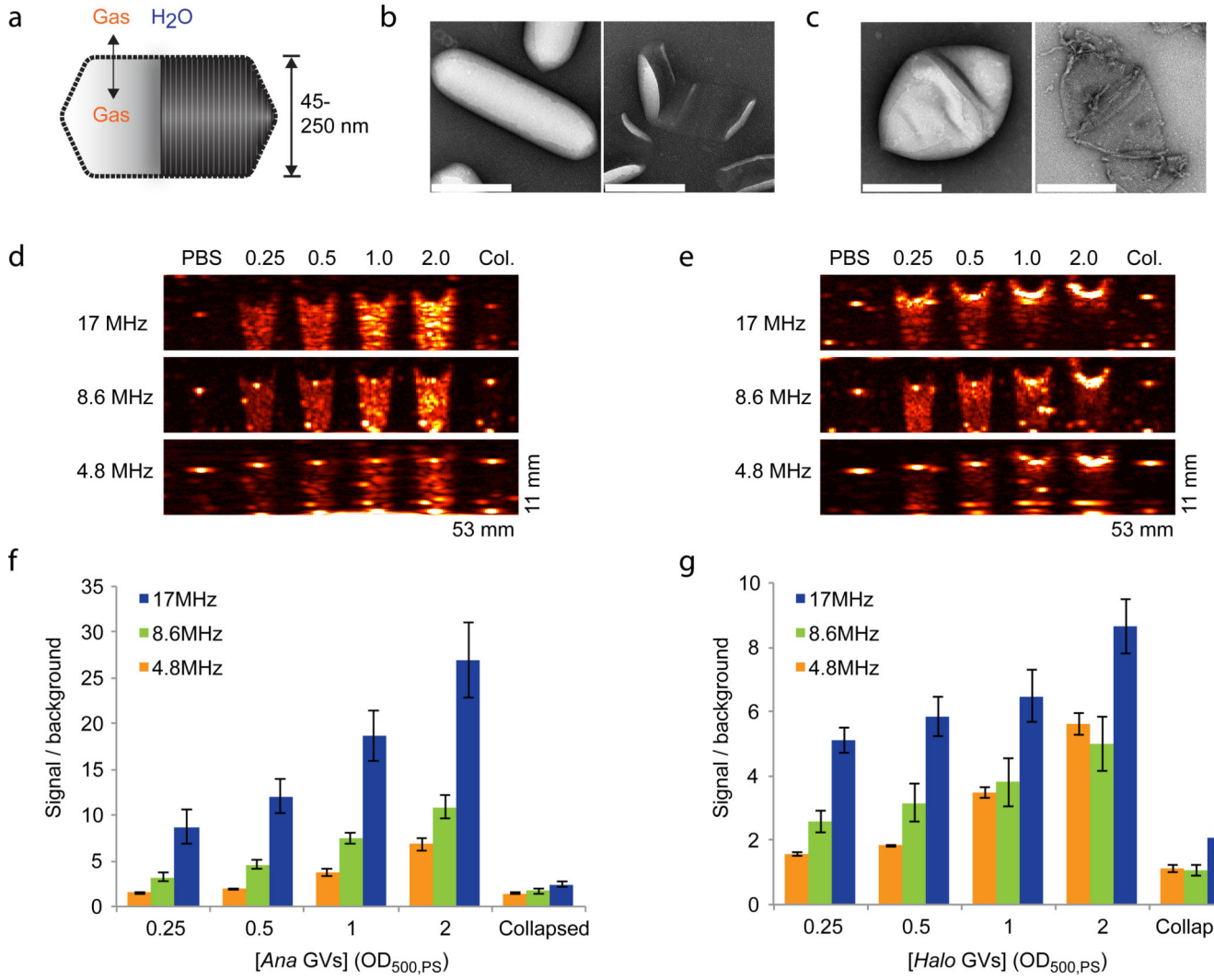

Figure 1. Gas vesicles produce ultrasound contrast

a, Diagram of a gas vesicle: a hollow gas nanocompartment (solid shading) surrounded by a gas-permeable protein shell (ribbed shading). **b**, TEM images of intact (left) and hydrostatically collapsed (right) *Ana* GVs. **c**, TEM images of intact (left) and collapsed (right) *Halo* GVs. All scale bars 200 nm. **d**, Ultrasound images of a gel phantom containing PBS buffer, *Ana* GVs at optical densities ranging from OD 0.25 to 2 (concentrations of 150 pM to 1.2 nM) or collapsed *Ana* GVs (OD 2.0). Images were acquired at multiple frequencies, as indicated. **e**, Ultrasound images of a gel phantom containing PBS buffer, *Halo* GVs at optical densities ranging from OD 0.25 to 2 (concentrations of 5 to 40 pM) or collapsed *Halo* GVs (OD 2.0). Conversion between OD, molar concentration and gas volume fraction is described in the Methods. **f**, Total backscattered signal relative to PBS at each frequency and *Ana* GV concentration (N=4 per sample). **g**, Total backscattered signal relative to PBS at each frequency and *Halo* GV concentration (N=4 per sample). Detailed image acquisition and analysis parameters are provided in Supplementary Table S1; colour maps for ultrasound images in Supplementary Fig. S9. The size of each field of view is indicated in the lower right corner of the image. All error bars represent ± SEM.

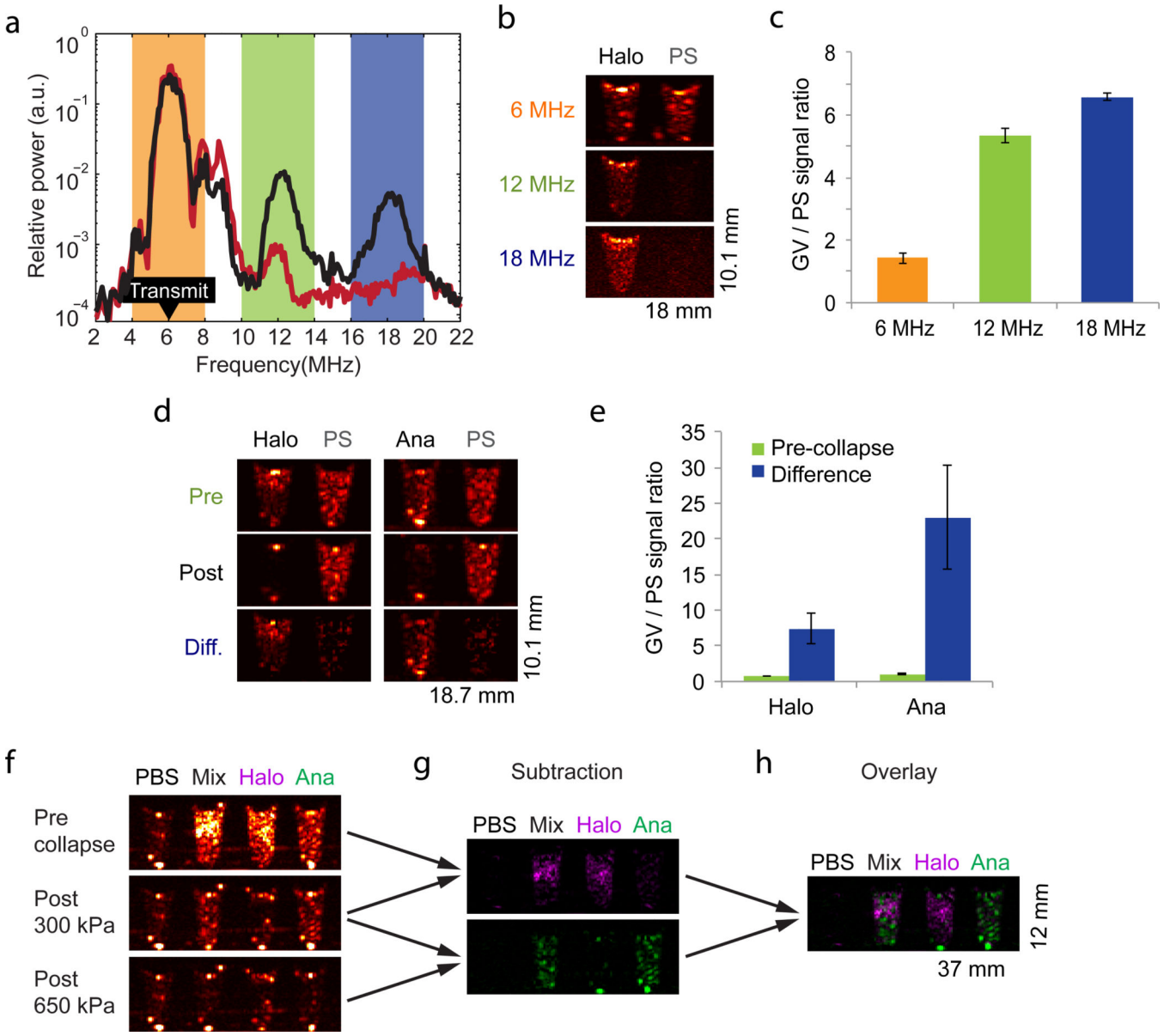

Figure 2. Non-linear imaging and genetic diversity enable enhanced contrast specificity and selective disruption imaging

a, Power spectrum of signal backscattered from *Halo* GVs (black) and 4.78 μm polystyrene (PS) microspheres (red) in response to 6 MHz transmitted pulses (peak amplitude 98 kPa, labeled “Transmit” in the figure), Each point on the spectrum represents an average of 48 points from 3 samples (16 points per sample). The orange, green and blue highlights correspond to frequency bands used to generate the images in (b). **b**, Ultrasound images of *Halo* GVs and PS microspheres acquired with 6 MHz transmission and band-pass filtered around 6, 12 and 18 MHz. **c**, Ratio of total backscattered signal from *Halo* GVs and PS microspheres after filtering at the indicated frequencies (N=4). **d**, Ultrasound images of *Halo* GVs, *Ana* GVs and PS microspheres at 8.6MHz acquired before (Pre) and after (Post) destructive collapse with 650 kPa insonation, and the difference (Diff.) between these

images. **e**, Ratio of total backscattered signal from GVs and PS microspheres in pre-collapse and difference images (N=4). The concentrations used in (a)-(e) were OD 0.5 *Halo* GVs, OD 2.0 *Ana* GVs and *0*.83% w/v polystyrene. **f**, Ultrasound images of a phantom containing wells with PBS, a mixture of *Ana* and *Halo* GVs, or each type of GVs on its own (all GVs at OD 1.0 in PBS), acquired at 8.6 MHz. Top: before collapse. Middle: after collapse at 300 kPa. Bottom: after collapse at 650 kPA. **g**. Top: difference between the top and middle images in (f), Bottom: difference between the middle and bottom images in (f). **h**. Overlay of the two images in (g). Detailed image acquisition and analysis parameters are provided in Supplementary Table S1; colour maps for ultrasound images in Supplementary Fig. S9. The size of each field of view is indicated in the lower right corner of the image. All error bars represent ± SEM.

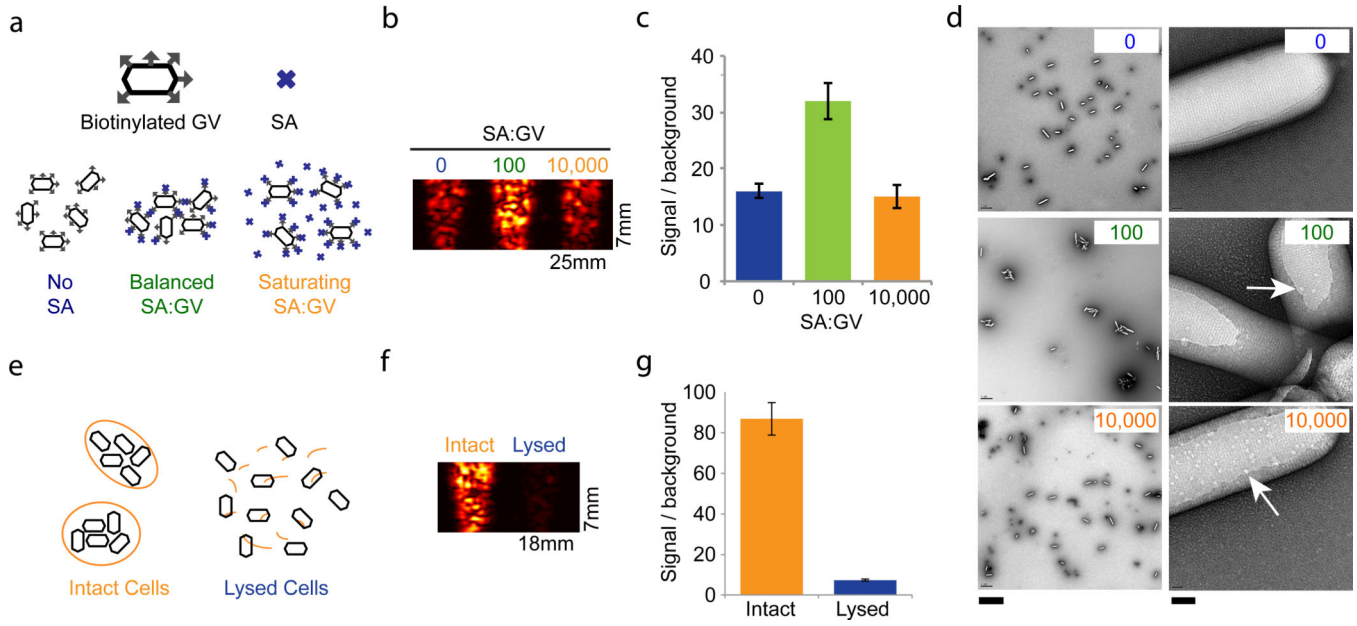

Figure 3. Gas vesicles act as biomolecular sensors and report cellular integrity

a, Illustration of predicted aggregation interactions between surface-biotinylated GVs (hexagons with gray arrows) and streptavidin (SA) at different SA:GV ratios. **b**, 17 MHz image of OD 1.0 biotinylated *Ana* GVs mixed with the indicated ratio of SA. **c**, Integrated signal intensity relative to phantom background corresponding to the SA:GV conditions in (b) (N=4 per condition). **d**, TEM images of *Ana* GVs incubated with SA at the indicated molar ratios on the top right hand corner of each panel. At the higher magnification (right), arrows indicate apparent SA molecules on the GV surface. Scale bars 2 μm (left) and 40 nm (right). **e**, Illustration of GVs (black hexagons) confined inside intact cells (orange) or released following lysis. **f**, Ultrasound image (17 MHz pulses) of *Ana* cells treated with water (intact) or with 25% sucrose (lysed). **g**, Integrated signal intensity relative to phantom background for intact and lysed cells (N=4 per condition). Detailed image acquisition and analysis parameters are provided in Supplementary Table S1; colour bars for ultrasound images in Supplementary Fig. S9. The size of each field of view is indicated in the lower right corner of the image. All error bars represent ± SEM.

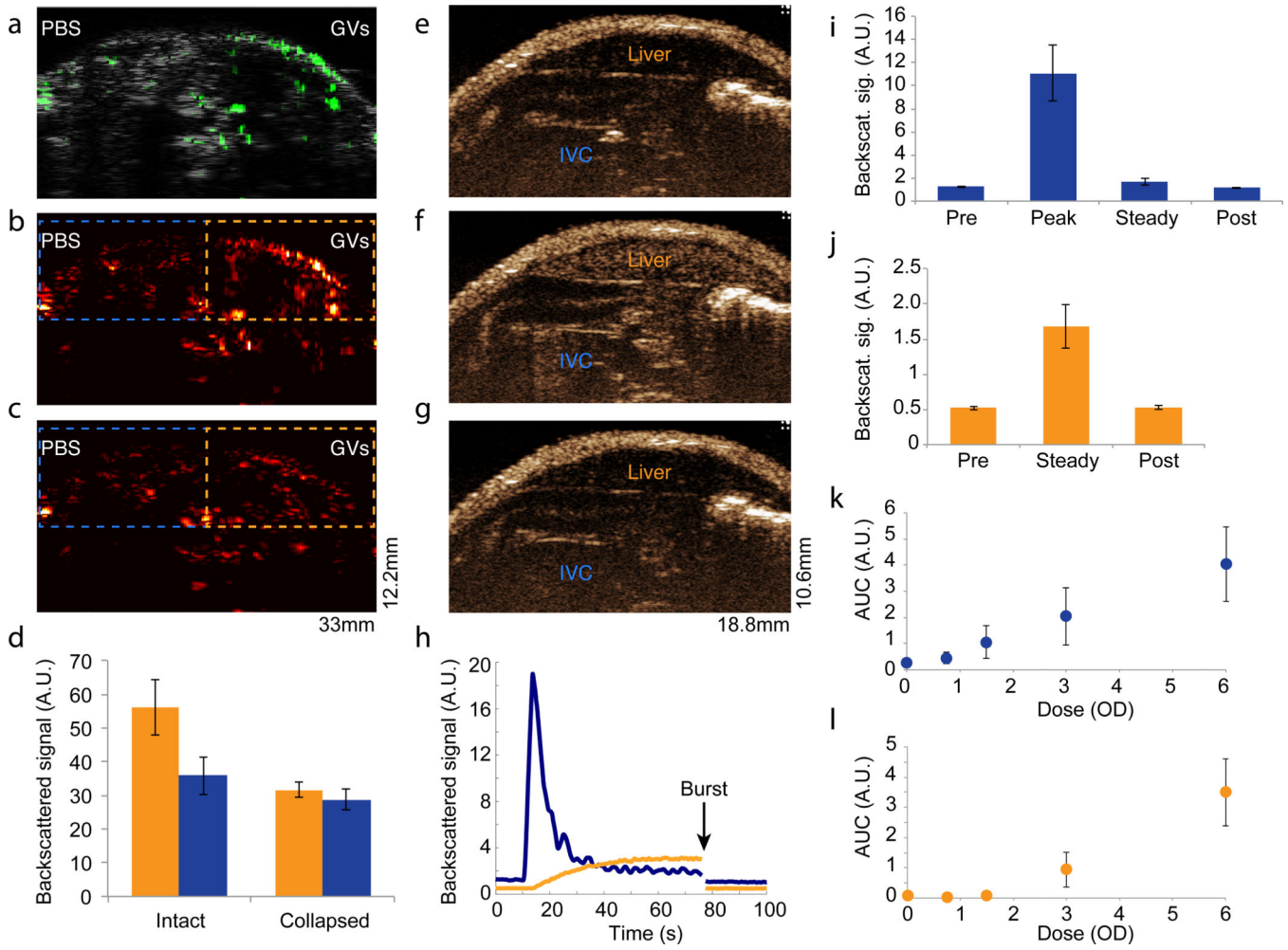

Figure 4. Gas vesicles produce ultrasound contrast *in vivo*

a, Overlay of second harmonic image (6 MHz pulses) in green on a grayscale broadband anatomical image of mouse lower abdomen injected subcutaneously with 150 μL OD 6.0 *Halo* GVs on the right side and 150uL PBS on the left side. **b–c**, Second harmonic ultrasound image before (b) and after (c) GV collapse with destructive insonation (650 kPa). Dashed outlines show regions of interest (ROI) used to quantify signals. **d**. Total back-scatted second harmonic signal from ROIs covering GV-injected (orange) and PBS-injected (blue) tissues, before and after collapse (N=5). **e–g**. Non-linear contrast images acquired using a high-frequency ultrasound scanner system (operating at 18 MHz and 2% power) of SCID nude mice infused intravenously with 50 μL OD 6.0 *Halo* GVs. The images show contrast at 4.5 seconds (e) and 64 seconds (f) after the start of infusion, or after the application of a burst pulse (g). The locations of the inferior vena cava (IVC) and liver are indicated with labels. **h**. Time course of the smoothed average non-linear signal in the IVC (blue) and liver (orange) during infusion. **i**. Mean average signal intensity in the IVC before (pre) during (peak) and after (steady) infusion, and after the burst pulse (post) (N=5). **j**. Mean average signal intensity in the liver before (pre) and after (steady) infusion, and after the burst pulse (post) (N=5). **k–l**. Dose-response relationship of 50 μL *Halo* GVs infused at OD 0 – 6.0 determined from the area under the curve (AUC) of average contrast in the IVC

(k) and liver (l) (N=5). Detailed image acquisition and analysis parameters are provided in Supplementary Table S1; colour maps for ultrasound images in Supplementary Fig. S9. The size of each field of view is indicated in the lower right corner of the image. All error bars represent ± SEM.